Int j simul model 24 (2025) 4, 706-717
Original scientific paper

CFD SIMULATION OF WIND-RAIN EFFECTS ON ULTRA-HIGH-SPEED TRAIN AERODYNAMICS AND SAFETY

Wang, J.*; Zhang, J. R.** & Liu, X. L.*

* School of Management and Engineering, Capital University of Economics and Business, No. 121 Zhangjiakou Rd., Beijing, P. R. China

** School of Mechanical, Electronic and Control Engineering, Beijing Jiaotong University, No.3 Shangyuancun, Beijing, P. R. China

E-Mail: wang.jie@cueb.edu.cn, jrzhang@bjtu.edu.cn, liuxinlei6080@163.com

Abstract

This study investigates the safety-critical speed thresholds of high-speed trains under extreme weather, particularly focusing on combined effects of heavy rainfall and crosswinds. A novel Lagrangian liquid film model, integrated with multiphase flow theory and RANS simulations, is developed to accurately capture wind-rain coupling effects. Through systematic analysis of varying rainfall intensities and crosswind speeds, key findings include: increasing rainfall intensity significantly amplifies aerodynamic parameters, with notable variations in roll and pitch moments under combined wind-rain conditions; the differential in water film thickness between windward and leeward surfaces increases by up to 1.55 times; at 500 km/h operation, safety margins remain above 40 % for rainfall ≤400 mm/h and crosswinds ≤15 m/s, whereas crosswinds exceeding 25 m/s cause lateral axle force to surpass the safety threshold by 4.68 %, compromising safety. This research establishes a theoretical framework for determining safe operational boundaries in extreme weather and provides critical technical support for formulating safety standards under adverse meteorological conditions.

(Received in July 2025, accepted in September 2025. This paper was with the authors 3 weeks for 3 revisions.)

Key Words: High-Speed Train, Wind-Rain Environment, Aerodynamic Parameters, Finite Element Simulation, Safety Threshold

1. INTRODUCTION

With China's rapid economic development, remarkable technological breakthroughs and continuous advancements have been achieved in high-speed rail systems. However, as operational speeds continue to increase, safety assurance remains the paramount concern in railway transportation [1]. Extreme weather events (e.g., gale-force winds and torrential rainfall) in specific climatic zones pose significant hazards to operational safety, frequently necessitating speed restrictions or even service suspensions. Consequently, investigating the safety-critical speed thresholds for high-speed trains under compounded adverse environmental conditions is of vital importance for ensuring secure and reliable operations at elevated velocities [2].

To address the impact of extreme wind and rain on the aerodynamic characteristics of high-speed trains, scholars generally build simulation models based on the theory of gas-liquid two-phase flow for analysis [3-5]. For the simulation of rainfall environment, the Euler-Lagrange method is commonly used to simulate the trajectory and mass transfer process of discrete particles in the fluid, i.e., raindrops, using the discrete phase model (DPM) [6-8]. Meanwhile, since the external flow field of high-speed trains presents typical turbulence characteristics, the Reynolds time-averaged method SST k-ω model is usually used to calculate it, which is able to effectively simulate the average flow characteristics, and also greatly reduce the more computational requirements and save computational time [9, 10].

Previous studies have systematically investigated the aerodynamic effects of rainfall on high-speed trains through various approaches. Sun et al. [11, 12] conducted comparative studies of uniform rainfall phase, M-P droplet spectrum, and Gamma droplet spectrum models, revealing that the uniform rainfall phase model yields higher aerodynamic forces and moments, while the Gamma spectrum model demonstrates greater sensitivity to velocity variations in aerodynamic characteristics. Zhang [13], Du and Ni [14] independently analysed aerodynamic force variations under rainfall conditions, both concluding that rainfall intensity has negligible impact on aerodynamic performance. Liu et al. [15] systematically examined the influence mechanisms of air density variation, droplet impingement, and water film formation on train aerodynamics during precipitation events. Simulation analysis possesses distinct advantages over the conduct of experiments, including reduced cost, shorter time requirements, and enhanced safety [16, 17]. Wu and Cao [18] identified that when exceeding critical Reynolds numbers, asymmetric vortices develop on one side of the train body, generating steady lift forces that significantly increase vibration probabilities. Complementing these findings, Xin et al. [19] demonstrated that rainfall-induced flow field alterations and water film formation exert more substantial influences on aerodynamic performance than droplet mass and impact forces alone.

Research on the aerodynamic effects of strong winds on high-speed trains has primarily employed experimental simulation and numerical modelling approaches. Peng et al. [20] investigated the CRH2 train model using combined wind tunnel tests and computational simulations to analyse rainfall impacts on critical aerodynamic parameters. Zhang et al. [21] conducted field experiments in wind-prone areas, demonstrating that crosswinds induce significant roll motion and nose sway, substantially compromising operational safety. Through comprehensive simulation models, Xi et al. [22], Luo et al. [23], and Zhao et al. [24] systematically examined high-speed train safety under crosswind conditions, revealing three key findings: (1) substantial increases in lateral force coefficients, (2) pressure zone displacement on the leading car with enhanced leeward-side negative pressure, and (3) a linear relationship between crosswind-induced lateral forces and maximum safe operating speeds.

Current research on ultra-high-speed trains' aerodynamic characteristics and operational safety under wind-rain conditions has achieved preliminary progress. However, existing studies exhibit these limitations. First, most focus on raindrop trajectory simulation, impact characteristics on train surfaces, and aerodynamic performance evaluation under crosswinds, with few addressing liquid film distribution on moving objects. Second, in-depth research is lacking on water film distribution patterns and dynamic flow characteristics across train surfaces in rainfall, particularly regarding liquid film effects' influence mechanisms on overall aerodynamics. Most importantly, no study has systematically correlated aerodynamic performance changes with operational safety assessments under combined wind-rain conditions.

This study takes a CR-series high-speed train as the research object, aiming to identify potential weak links in the train safety parameter system. Based on existing research findings, it comprehensively employs computational fluid dynamics theory, turbulence models, and the Lagrangian liquid film model to systematically analyse the distribution characteristics and dynamic evolution of liquid films on the train surface under different coupling conditions of rainfall intensity and crosswind speed, as well as varying operational speeds. By quantitatively investigating the coupling mechanism between liquid film effects on the train surface and crosswind aerodynamic loads in wind-rain environments, this study thoroughly explores the speed threshold range for safe train operation under rainfall conditions. Unlike previous works, this study systematically links wind-rain-induced liquid film effects to both aerodynamic loads and safety thresholds, providing an integrated simulation framework for safety evaluation under extreme weather conditions. Our framework extends simulation modelling of train aerodynamics by incorporating wind-rain coupling with liquid film evolution, enabling more realistic safety assessments. The research results not only provide a theoretical basis for determining the operational safety boundaries of high-speed trains under extreme rainfall but also offer important references for studies on ensuring train operational safety in adverse weather conditions.

2. SIMULATION THEORY AND MODEL ESTABLISHMENT

2.1 Theoretical model

After a certain period of rainfall, droplets form a liquid film on the surface of the high-speed train. Therefore, a liquid film model must be established to describe the process of raindrop impact on the liquid film. This study introduces a liquid film modelling method based on the Lagrangian approach to investigate the characteristics of water film formation on the exterior surface of the high-speed train under rainfall conditions.

The model treats the liquid as a system composed of numerous fine particles and precisely tracks and calculates the motion trajectories and interactions of these particles on the solid surface. The Lagrangian model encompasses several key processes, including the deposition of liquid particles on the surface to gradually form a liquid film, the splashing phenomenon caused by contact with the wall, and the dynamic behaviour of liquid film flow along the surface, as illustrated in Fig. 1 [25, 26].

The interaction between droplets and the structural surface is closely related to a critical Weber number (We), which represents the ratio of inertial forces to surface tension forces acting on a droplet. A higher We indicates greater tendency for droplet deformation, splashing, or breakup upon impact. The Ohnesorge number (Oh), on the other hand, relates viscous forces to inertial and surface tension forces, helping to predict droplet behaviour such as spreading or recoil. The entire process of raindrop particles accumulating on the train surface and evolving into a liquid film must still adhere to the fundamental physical laws of mass and momentum conservation. The expressions for the Weber number (We) and Ohnesorge number (Oh) are:

$$We = \frac{\rho_p |u - u_p| D_p}{\sigma} \tag{1}$$

$$Oh = \frac{\mu_p}{\sqrt{\rho_p \sigma D_p}} \tag{2}$$

where: ρ_p denotes the fluid density (kg/m^3); σ represents the surface tension coefficient; D_p refers to the raindrop particle diameter (mm); μ_p stands for the dynamic viscosity coefficient.

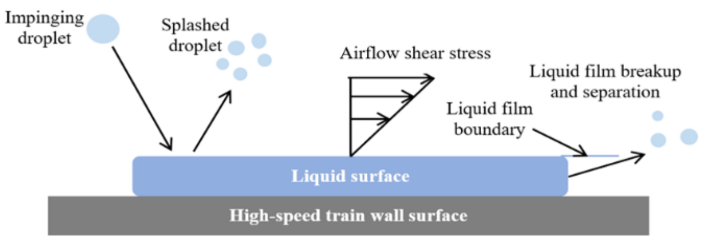

Figure 1: Dynamics of liquid film interaction processes.

2.2 Train model

(1) Geometric model

A two-car formation model (head car + tail car) was established to characterize the flow field states of typical vehicle sections during simulation studies. The car body measures 4.05 m in height and 3.38 m in width. Each car has a length of 25.7 m, including a streamlined section of 12 m, resulting in a total train length of 51.4 m. To meet the research requirements, detailed features of the train surface and tracks were simplified and processed into geometric bodies composed of smooth curved surfaces [27]. The established model complies with the EN 14067-6:2010 standard, as shown in Fig. 2.

Figure 2: Geometric model of the train: train side view (left), train front view (right).

(2) Mesh generation

The train mesh employs a hybrid grid system combining hexahedral and tetrahedral elements, with particular refinement applied to the geometrically complex head and tail sections where significant flow variations occur to enhance simulation accuracy. The configuration features 10 prism layers initially applied to the vehicle surface (later increased to 12 boundary layers with a first-layer thickness of 1 mm), along with two refinement zones surrounding the train. Grid sizing parameters include a maximum surface element dimension of 100 mm, with volumetric elements ranging from 100 mm to 3 m in the fluid domain. The mesh architecture utilizes hexahedral elements as the primary components supplemented by polyhedral elements, as illustrated in Fig. 3.

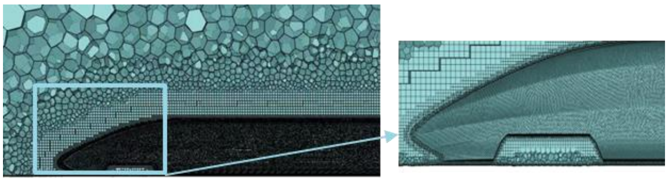

Figure 3: Mesh generation.

(3) Boundary conditions

The simulation domain was configured with dimensions of 551.4 m in length, 53.38 m in width, and 29.05 m in height. The train model was positioned 150 mm above the ground surface, with lateral offsets of 25 m from both side walls, while maintaining longitudinal offsets of 400 m from the front boundary and 100 m from the rear boundary of the computational domain.

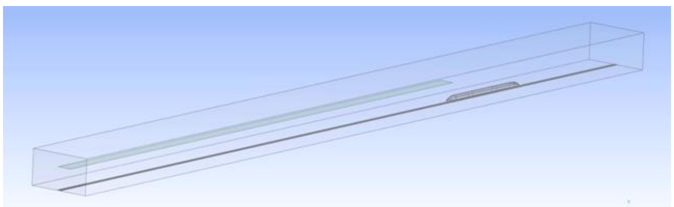

Figure 4: Computational domain configuration of the train.

The numerical simulation employed the following boundary condition configuration: The train body surface and domain bottom were set as solid walls, while the front boundary was specified as a velocity inlet and the rear boundary as a pressure outlet. Symmetry conditions were applied to the top and side boundaries. For the discrete phase modelling, escape boundaries were assigned to the inlet/outlet surfaces, with a trap boundary condition at the bottom. The train surfaces were treated as wall film boundaries to simulate liquid film accumulation from raindrop impingement. Raindrops entering the computational domain acquired horizontal velocity components through interaction with the inlet airflow. The rainfall plane was positioned 10 m above the train (parallel to the domain top), with dimensions of 390 m (length) × 20 m (width), offset by 5 m from the front boundary, 156.41 m from the rear boundary, 14.2 m above the ground, and 16.8 m from each side wall. This configuration ensured complete coverage of the train surface during precipitation simulation, with the rainfall plane indicated by the green region in Fig. 4.

2.3 Simulation parameters

This study selects 500 km/h as the ultimate operating speed for the high-speed train. Based on typical operational scenarios of high-speed trains and their suspension/velocity restriction standards under strong wind conditions, two crosswind velocities of 15 m/s and 25 m/s were chosen, representing Beaufort scale levels 7 and 9 respectively. Fig. 5 illustrates the resultant wind velocity diagram, where the simulation assumes a stationary train relative to the ground, with incoming airflow approaching at a velocity equal in magnitude but opposite in direction to the train's speed. The resultant wind velocity vector is obtained by combining the head-on airflow and crosswind components, forming an angle α (termed yaw angle) [28] between the resultant flow direction and the train's longitudinal axis. The derivation of angle α follows the formula [29]:

$$\alpha = tan^{-1}[(W\,sin\beta) / (v + W\,cos\beta)] \tag{3}$$

where v denotes train speed, W represents crosswind velocity, and u is the resultant velocity. With the crosswind defined as perfectly lateral ($\beta = 90°$), Eq. (3) simplifies to:

$$\alpha = tan^{-1}(u/v) \tag{4}$$

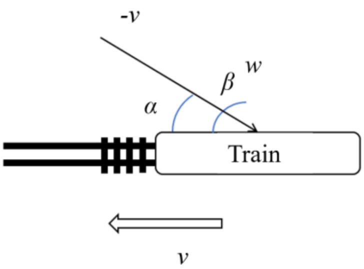

Figure 5: Schematic diagram of resultant wind velocity.

Based on the rainfall intensity classification standards officially issued by the China Meteorological Administration, this study selected precipitation rates of 200 mm/h and 400 mm/h. The raindrop distribution parameters for these rainfall intensities were calculated using the Gamma raindrop size distribution model, with the specific configuration parameters shown in Table I.

Table I: Rainfall parameters.

Rainfall intensity (mm/h)	Droplet diameter (mm)	Terminal velocity (m/s)	Mass flow rate (kg/s)
200	3.43	8.54	163.2
400	4.01	8.87	378.8

3. AERODYNAMIC PERFORMANCE OF TRAINS UNDER WIND-RAIN CONDITIONS

3.1 Liquid film distribution characteristics

Fig. 6 illustrates the temporal evolution of liquid film distribution characteristics on the train surface under operating conditions of 500 km/h train speed, 15 m/s crosswind velocity, and 400 mm/h rainfall intensity. The results demonstrate that under coupled wind-rain effects, aerodynamic flow deflects raindrops predominantly toward the roof and windward side, where initial liquid film accumulation occurs. Progressive precipitation leads to gradual thickening of the roof film, reaching relative stability at $t = 7$ s. Under combined influences of wind shear and resultant flow velocity, the liquid film migrates rearward along the roof, maintaining alignment with the primary flow direction. At $t = 3$ s, minimal film formation is observed only near the leading-edge windows on the leeward side, while by $t = 7$ s the windward surface achieves near-complete film coverage with subsequently increasing thickness. The liquid film exhibits gravitational drainage behaviour modulated by surface shear stresses, culminating in extensive leeward-side coverage by $t = 9$ s.

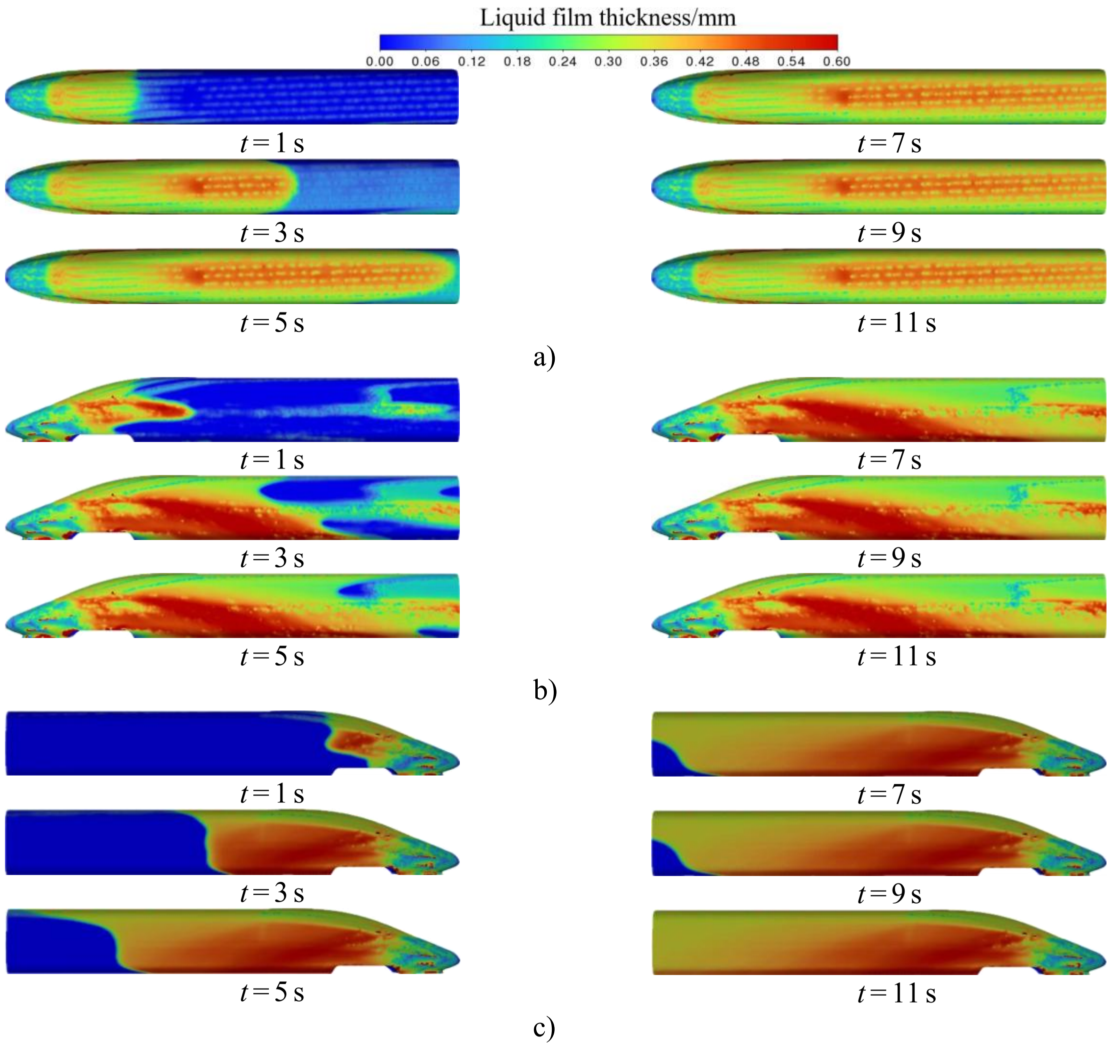

Figure 6: Variation of the liquid film thickness on the train body with time; a) Top-view liquid film distribution, b) Windward-side film thickness contour, c) Leeward-side film thickness contour.

3.2 Flow field characteristics

(1) Shear stress

Fig. 7 presents the surface shear stress distribution on the high-speed train at 500 km/h with 15 m/s crosswind under both dry conditions and 400 mm/h rainfall intensity. Comparative analysis reveals significantly higher shear stress magnitudes on the windward side versus the leeward side under identical environmental conditions. Notably, the maximum shear stress occurs at the rear section of the streamlined roof under 400 mm/h precipitation, exceeding dry-condition values. This phenomenon originates from the combined aerodynamic loading where the train's nose geometry focuses incoming airflow onto the roof-streamline transition zone. Fig. 7 c demonstrates substantially elevated shear stress at the windward-roof junction compared to other windward regions, causing partial liquid film detachment and downstream migration under shear-airflow interaction, resulting in localized thinning. Fig. 7 d identifies three critical leeward stress concentration zones: (i) streamline-sidewall interface, (ii) nose section, and (iii) streamlined protrusions, all exhibiting reduced film thickness due to enhanced shear effects.

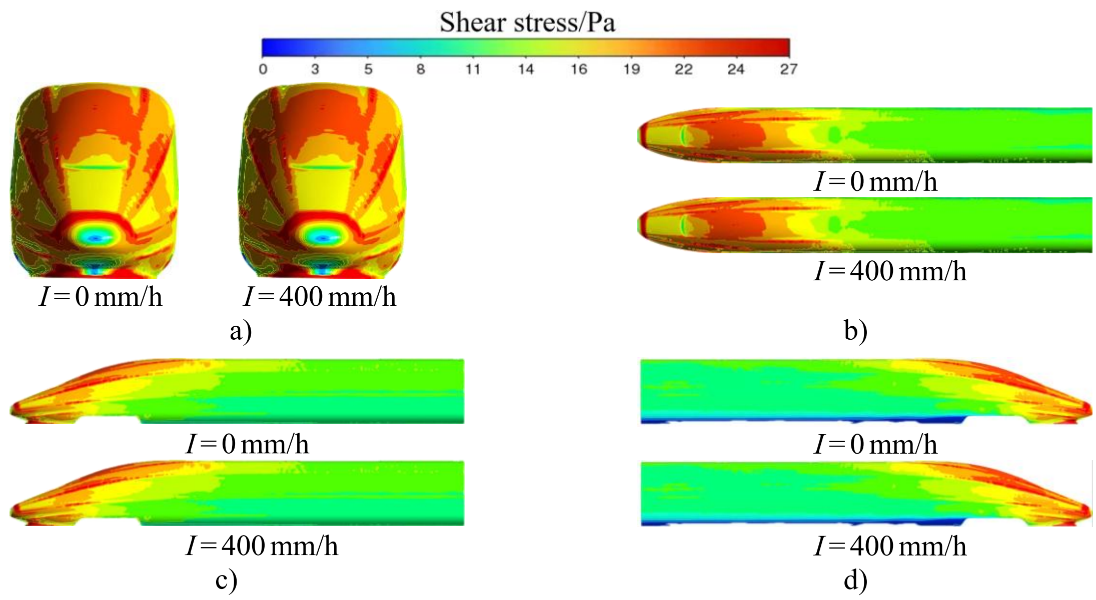

Figure 7: Shear stress on the train outer surface as a function of rainfall intensity; a) Frontal-view shear stress contour, b) Top-view shear stress contour, c) Windward-side shear stress contour, d) Leeward-side shear stress contour.

Fig. 8 presents the shear stress distribution along the roof centreline of the high-speed train at 500 km/h with 15 m/s crosswind under varying rainfall intensities. Analysis reveals a systematic increase in surface shear stress with higher precipitation rates, attributable to thickening liquid films that amplify air-liquid interface fluctuations. This interfacial instability enhances shear stress magnitude, consequently influencing the train's aerodynamic drag characteristics. The liquid film dynamics are governed by competing forces including surface tension, gravity, airflow shear stress, and wall friction, with aerodynamic shear and gravitational forces being the dominant factors. Under conditions of 500 km/h train speed, 400 mm/h rainfall intensity, and 11 s precipitation duration, the maximum film flow velocity reaches 33.48 m/s on the train surface.

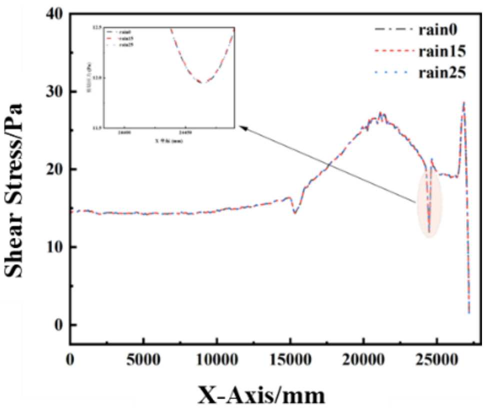

Figure 8: Shear stress distribution along roof centreline under varying rainfall intensities.

(2) Friction coefficient

Fig. 9 presents the surface friction coefficient distribution under crosswind conditions of 15 m/s at 500 km/h train speed, comparing dry conditions with 400 mm/h rainfall intensity. The analysis reveals significantly lower friction coefficients on the leeward side compared to the windward side under crosswind effects. Rainfall exposure induces moderate friction coefficient increases in three critical regions: (i) the rear roof section, (ii) windward surfaces, and (iii) streamlined protrusions. Quantitative measurements show the average surface friction coefficient rises from 0.00142 (dry) to 0.00167 (400 mm/h), representing a 17.6 % enhancement attributable to liquid film interaction effects.

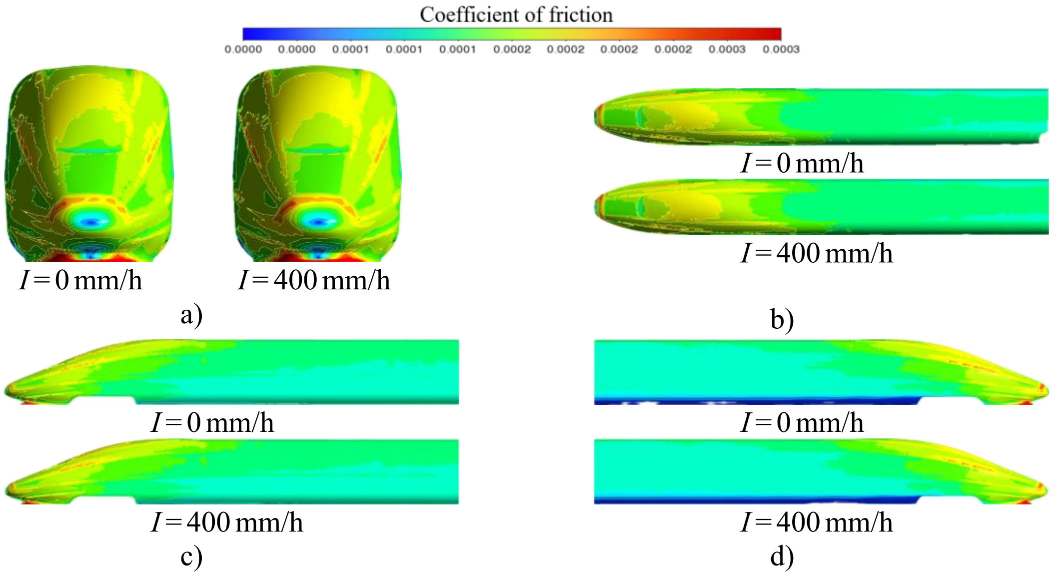

Figure 9: Friction coefficient on the train outer surface versus rainfall intensity; a) Leading car friction coefficient distribution, b) Leading car friction coefficient contour, c) Windward-side friction coefficient contour, d) Leeward-side friction coefficient contour.

Fig. 10 presents the surface friction coefficient distribution along the roof centreline at 500 km/h train speed with 15 m/s crosswind under varying rainfall intensities, where the abscissa origin (0 mm) corresponds to the leading car's rear end and 25700 mm indicates the nose tip position. The results demonstrate a systematic increase in both surface shear stress and friction coefficient with higher precipitation rates, attributable to liquid film formation that alters surface morphology. Specifically, the combined effects of aerodynamic shear and raindrop impacts generate micro-scale undulations and surface depressions in the liquid film, which disrupt the original aerodynamic smoothness and enhance surface roughness, thereby elevating the friction coefficient.

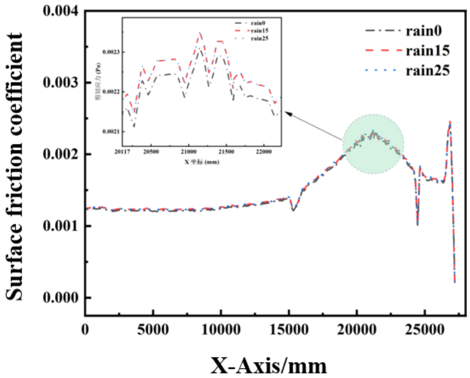

Figure 10: Surface friction coefficient distribution along roof centreline.

3.3 Aerodynamic parameters

Fig. 11 presents the variations of aerodynamic coefficients-including drag coefficient, lift coefficient, overturning moment coefficient, rolling moment coefficient, and pitching moment coefficient for a train operating under 400 mm/h rainfall intensity with varying crosswind velocities. The results demonstrate a positive correlation between crosswind magnitude and aerodynamic coefficients under identical precipitation conditions. Notably, the side force coefficient, lift coefficient, and pitching moment coefficient exhibit particularly strong sensitivity to crosswind variations, with all three parameters increasing by over 100 % when crosswind velocity rises from 0 to 15 m/s under rainy conditions.

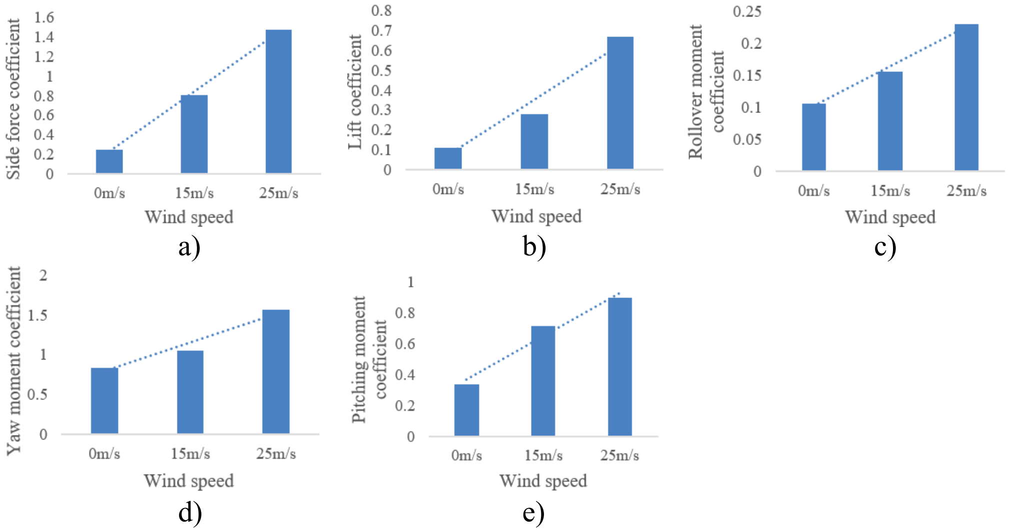

Figure 11: Aerodynamic coefficients of the train; a) Side force coefficient, b) Lift coefficient, c) Rollover moment coefficient, d) Yaw moment coefficient, e) Pitching moment coefficient.

4. TRAIN SAFETY PERFORMANCE IN WIND-RAIN ENVIRONMENTS

4.1 Impact of rainfall intensity on train safety

Fig. 12 illustrates the influence of varying rainfall intensities on train safety metrics at a constant speed of 500 km/h with 15 m/s crosswind. The data demonstrate progressive increases in derailment coefficient, wheel load reduction rate, axle lateral force, and wheel-rail transverse force with higher precipitation rates. This confirms that under fixed train speed and crosswind conditions, all critical safety indicators exhibit positive correlations with rainfall intensity enhancement. These quantitative relationships provide a basis for establishing graded rainfall intensity warnings and corresponding speed control strategies in operational safety management.

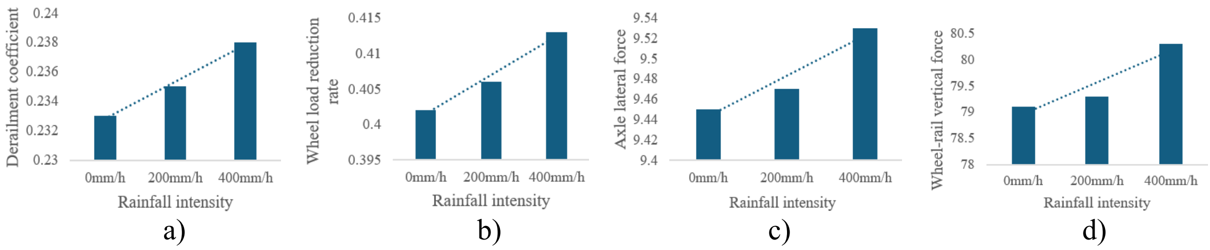

Figure 12: Variations of safety indicators under different rainfall conditions; a) Derailment coefficient, b) Wheel load reduction rate, c) Axle lateral force, d) Wheel-rail vertical force.

Under conditions of 400 mm/h rainfall intensity and 25 m/s crosswind speed, the measured axle lateral force reaches 16.75 kN, exceeding the safety operational threshold by 4.68 %. While other parameters remain within safe limits, these findings demonstrate that trains should implement speed restrictions or service suspension when encountering 400 mm/h precipitation combined with 25 m/s winds to ensure operational safety. Specifically, this combination of weather conditions should trigger mandatory speed reduction below 400 km/h or complete line suspension according to the risk classification framework proposed in this study.

4.2 Influence of crosswind speed on train safety performance

Fig. 13 demonstrates the influence of crosswind speed variation on train safety metrics under constant operational conditions of 500 km/h train speed and 400 mm/h rainfall intensity. The data reveal progressive increases in derailment coefficient (*Q/P*), wheel load reduction rate ($\Delta P/P$), axle lateral force (*Y*), and wheel-rail transverse force with escalating crosswind velocities. This confirms that while maintaining fixed train speed and precipitation intensity, all critical safety indicators exhibit significant positive correlations with increasing crosswind magnitude. These trends align with field test observations by Zhang et al. [21], who reported a 41 % increase in lateral wheelset force under strong crosswinds, confirming the simulation's predictive capability for safety-critical scenarios. The established correlation between crosswind speed and safety parameters enables the development of predictive models for real-time risk assessment during operations.

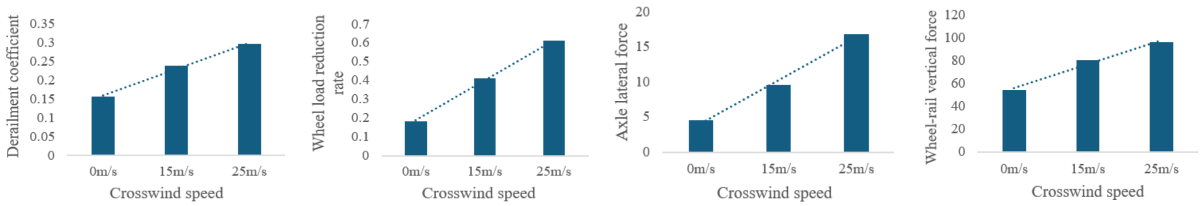

a) b) c) d)

Figure 13: Variations of safety indicators under different crosswind conditions; a) Derailment coefficient, b) Wheel load reduction rate, c) Axle lateral force, d) Wheel-rail vertical force.

Under operational conditions of 500 km/h train speed, 400 mm/h rainfall intensity, and 15 m/s crosswind, all safety indicators remain within prescribed thresholds: derailment coefficient (0.238), wheel load reduction rate (0.413), axle lateral force (9.53 kN), and wheel-rail vertical force (80 kN). Notably, both derailment coefficient and vertical force remain below 50 % of their safety limits, while load reduction reaches 51.6 % and lateral force attains 60 % of respective thresholds, maintaining substantial safety margins. These results demonstrate that ultra-high-speed trains can operate safely at 500 km/h in combined wind-rain environments with precipitation ≤ 400 mm/h and crosswinds ≤ 15 m/s. Based on these findings, we propose a multi-level operational protocol: (1) Normal operation (green alert) for conditions within these parameters; (2) Speed restriction to 400 km/h (yellow alert) when either rainfall exceeds 400 mm/h or crosswinds exceed 15 m/s; (3) Line suspension (red alert) when both rainfall exceeds 400 mm/h and crosswinds exceed 25 m/s, or when any safety indicator exceeds 85 % of its threshold value.

5. CONCLUSION

This study presents the first integrated analysis of wind-rain-induced liquid film effects on aerodynamic performance and operational safety for 500 km/h ultra-high-speed trains, employing a novel Lagrangian liquid film model coupled with RANS-based multiphase flow simulations. The key findings demonstrate that:

(1) Rainfall intensity critically amplifies liquid film thickness disparity (increased by up to 1.55 times between the windward and leeward surfaces), directly increasing shear stress and aerodynamic drag fluctuations;

(2) Strong crosswinds (25 m/s) combined with heavy rainfall (400 mm/h) cause asymmetric pressure distribution and lateral instability, with axle lateral force exceeding safety thresholds by 4.68 %;

(3) Safe operation is achievable at 500 km/h under rainfall ≤ 400 mm/h and crosswinds ≤ 15 m/s, with all safety margins exceeding 40 %.

These results provide quantitative guidance for establishing extreme-weather operational standards and real-time safety management protocols for ultra-high-speed railways. The proposed simulation framework offers a validated tool for evaluating coupled environmental risks. Future work will focus on experimental validation through wind tunnel tests, extension to 3D train formations, and investigation of additional weather scenarios (e.g., snow, hail) to enhance model generality and operational applicability.

REFERENCES

[1] Liu, Y.; Liang, B.; Zhao, N, Y.; Wei, S. (2017). Dynamic characteristics of coupled vehicle-track-tunnel interaction system, *International Journal of Simulation Modelling*, Vol. 16, No. 4, 685-669, doi:10.2507/IJSIMM16(4)8.401

[2] Xing, Y. Z.; :Guo, X. Y.; Si, Q. M.; Zeng, Z.; Guo, Y. Y. (2025). Emergency decision simulation for urban rail transit during rainstorm floods, *International Journal of Simulation Modelling*, Vol. 24, No. 3, 449-460, doi:10.2507/IJSIMM24-3-733

[3] Fatahian, H.; Salarian, H.; Nimvari, M. E.; Khaleghinia, J. (2020). Computational fluid dynamics simulation of aerodynamic performance and flow separation by single element and slatted airfoils under rainfall conditions, *Applied Mathematical Modelling*, Vol. 83, 683-702, doi:10.1016/j.apm.2020.01.060

[4] Gholamalipour, P.; Hua, G.; Stathopoulos, T. (2024). Impact of upstream buildings on Wind-Driven Rain Loading: refining obstruction factor in ISO semi-empirical model based on CFD, *Journal of Building Engineering*, Vol. 97, Paper 110717, 24 pages, doi:10.1016/j.jobe.2024.110717

[5] Gholamalipour, P.; Hua, G.; Stathopoulos, T. (2024). CFD modeling of Wind-Driven Rain (WDR) on a mid-rise building in an urban area, *Journal of Wind Engineering and Industrial Aerodynamics*, Vol. 245, Paper 105637, 17 pages, doi:10.1016/j.jweia.2023.105637

[6] Zhao, P.; Gao, J. (2024). Numerical simulation analysis of rainwater contamination on vehicle side windows, *Acta Aerodynamica Sinica*, Vol. 42, No. 7, 86-102, doi:10.7638/kqdlxxb-2024.0018

[7] Fu, S.; Guo, X. Y.; Dong, L. H.; Sheng, K.; Sun, A. (2022). Numerical simulation of migration laws of dense particle flow in pipelines, *International Journal of Simulation Modelling*, Vol. 21, No. 1, 89-100, doi:10.2507/IJSIMM21-1-592

[8] Yu, M.-G.; Li, H.-Q.; Liu, J.-L.; Li, T. (2020). Study on the aerodynamic performance of the high-speed train under strong wind and rainfall environment, *Journal of Mechanical Engineering*, Vol. 56, No. 4, 185-192, doi:10.3901/JME.2020.04.185

[9] Cheng, K.; Qi, W.-Z. (2024). Simulation and analysis of aerodynamic forces on high-speed trains under crosswind conditions, *Mechanical & Electrical Engineering Technology*, Vol. 53, No. 7, 201-204+216, doi:10.3969/j.issn.1009-9492.2024.07.042

[10] Montenegro, P. A.; Barbosa, D.; Carvalho, H.; Calçada, R. (2020). Dynamic effects on a train-bridge system caused by stochastically generated turbulent wind fields, *Engineering Structures*, Vol. 211, Paper 110430, 16 pages, doi:10.1016/j.engstruct.2020.110430

[11] Sun, Z.-B.; Du, L.-M. (2018). Impact of rainfall on aerodynamic characteristics of high-speed trains based on Gamma raindrop spectrum, *Journal of Dalian Jiaotong University*, Vol. 39, No. 6, 24-29, doi:10.13291/j.cnki.djdxac.2018.06.006

[12] Sun, Z.-B. (2019). *Influence of Wind-Rain Coupling Effects on Operational Safety of High-Speed Trains*, Dalian Jiaotong University, Dalian (in Chinese)

[13] Zhang, M. (2012). *Numerical Simulation and Analysis of Multiphase Flow for High-Speed Trains Based on Particle Tracking Model*, Zhejiang University, Hangzhou (in Chinese)

[14] Du, L.-M.; Ni, S.-L. (2016). Influence of aerodynamic characteristics of a high-speed train under rain and lower atmospheric boundary layer crosswind conditions, *Journal of Dalian Jiaotong University*, Vol. 37, No. 5, 56-61, doi:10.13291/j.cnki.djdxac.2016.05.011

[15] Liu, Q.-K.; Qiao, F.-G.; Du, Y.-L. (2007). Preliminary study on the effect of rainfall on aerodynamic characteristics of basic components, *Journal of Shijiazhuang Railway Institute (Natural Science Edition)*, Vol. 20, No. 4, 14-18+44, doi:10.13319/j.cnki.sjztddxxbzrb.2007.04.001

[16] Si, Q. M.; Zhao, Y. H.; Huo, S.; Fu, S.; Zhang, H. T. (2024). A simulation method for fireproof space design in aviation airport terminals, *International Journal of Simulation Modelling*, Vol. 23, No. 4, 644-655, doi:10.2507/IJSIMM23-4-703
[17] Yehoshua, A.; Bechar, A.; Cohen, Y.; Shmuel, L.; Edan, Y. (2023). Dynamic sampling algorithm for agriculture-monitoring ground robot, *International Journal of Simulation Modelling*, Vol. 22, No. 3, 392-403, doi:10.2507/IJSIMM22-3-646
[18] Wu, Z.; Cao, Y. (2015). Numerical simulation of flow over an airfoil in heavy rain via a two-way coupled Eulerian–Lagrangian approach, *International Journal of Multiphase Flow*, Vol. 69, 81-92, doi:10.1016/j.ijmultiphaseflow.2014.11.006
[19] Xin, D.-B.; Li, H.; Ou, J.-P.; Wang, L.; Chen, D.-Y. (2013). Experimental study on flutter stability of a long-span bridge subject to wind-rain actions, *Science China (Technological Sciences)*, Vol. 56, No. 8, 2089-2098, doi:10.1007/s11431-013-5269-3
[20] Peng, Y.-H.; He, X.-H.; Jing, H.-Q.; Xie, N.-C. (2021). Wind tunnel experimental study on aerodynamic performance of high-speed trains under coupled wind and rain conditions, *Journal of Central South University (Science and Technology)*, Vol. 52, No. 9, 3353-3365, doi:10.11817/j.issn.1672-7207.2021.09.037
[21] Zhang, Z.-C.; Qu, D.; Li, G.; Chu, G. F.; Zhu, H. L; He, D.-H. (2023). Experimental study on operational safety and dynamic characteristics of locomotive vehicles under crosswind conditions, *Railway Locomotive & Car*, Vol. 43, No. 3, 9-16, doi:10.3969/j.issn.1008-7842.2023.03.02
[22] Xi, Y.-H.; Mao, J.; Gao, L.; Yang, G.-W.; Qu, W.-Q. (2012). Study on speed limit for safe operation of high-speed trains under crosswind conditions, *Journal of the China Railway Society*, Vol. 34, No. 6, 8-14, doi:10.3969/j.issn.1001-8360.2012.06.002
[23] Luo, W.-H.; Li, Z.-Y.; Zhang T. (2022). Influence of different track types on aerodynamic characteristics of high-speed trains in wind-sand environments, *Railway Standard Design*, Vol. 66, No. 11, 36-42, doi:10.13238/j.issn.1004-2954.202108030001
[24] Zhao, C.-H.; Li, D.-C.; Li, W.-H.; Jia, R.-G.; Yan, R.-J. (2024). Research on operational safety of high-speed trains under crosswind conditions, *Science Technology and Engineering*, Vol. 24, No. 30, 13136-13144, doi:10.12404/j.issn.1671-1815.2307904
[25] Fu, J.-L.; Sun, X.-F.; Guo, Y.-X.; Chen, X.-W.; Cheng, H.-D. (2025). D'Alembert Lagrange principle and dynamic equations of flexible object systems, *International Journal of Non-Linear Mechanics*, Vol. 178, Paper 105221, 15 pages, doi:10.1016/j.ijnonlinmec.2025.105221
[26] Yu, J.-Y.; Galindo-Lopez, S.; Cleary, M. J. (2025). A coupled Eulerian–Lagrangian approach with explicit volume diffusion subgrid closures for jet breakup and atomisation, *Applications in Energy and Combustion Science*, Vol. 23, Paper 100350, 17 pages, doi:10.1016/j.jaecs.2025.100350
[27] Jing, J.-E.; Gao, G.-J. (2013). Numerical simulation of forces on high-speed trains under combined wind and rain conditions, *Journal of Railway Science and Engineering*, Vol. 10, No. 3, 99-102, doi:10.19713/j.cnki.43-1423/u.2013.03.020
[28] Li, X.-B.; Yang, Z.; Zhang, J.-Y.; Zhang, W.-H. (2009). Aerodynamic performance of high-speed trains in strong winds, *Journal of Traffic and Transportation Engineering*, Vol. 9, No. 2, 66-73, doi:10.19818/j.cnki.1671-1637.2009.02.012
[29] Ran, Z. W. (2021). *Research on Running Safety and Comprehensive Evaluation System of High-Speed Trains on Bridges under Wind and Rain Environments*, Dissertation Thesis, Southwest Jiaotong University, Chengdu (in Chinese)